

Cryo-EM structure of the human Sirtuin 6-nucleosome complex

Short Title: Cryo-EM structure of the SIRT6-nucleosome complex

Un Seng Chio^{1,2,3†}, Othman Rechiche^{1,2,†}, Alysia R. Bryll^{4,5†}, Jiang Zhu^{1,2}, Jessica L. Feldman⁴,
Craig L. Peterson^{4*}, Song Tan^{1,2*}, Jean-Paul Armache^{1,2*}

¹Center for Eukaryotic Gene Regulation, Department of Biochemistry and Molecular Biology, Pennsylvania State University, University Park, PA 16802, USA.

²The Huck Institutes of the Life Sciences, Pennsylvania State University, University Park, PA 16802, USA.

³Department of Biochemistry and Biophysics, University of California San Francisco, San Francisco, CA 94152, USA.

⁴Program in Molecular Medicine, University of Massachusetts Medical School, Worcester, MA 01605, USA.

⁵Medical Scientist Training Program, University of Massachusetts Medical School, Worcester, MA 01605.

*Corresponding authors:

craig.peterson@umassmed.edu

sxt30@psu.edu

jza449@psu.edu

†These authors contributed equally to this work

27 Abstract

28 Sirtuin 6 (SIRT6) is a multifaceted protein deacetylase/deacylase and a major target for small-
29 molecule modulators of longevity and cancer. In the context of chromatin, SIRT6 removes acetyl
30 groups from histone H3 in nucleosomes, but the molecular basis for its nucleosomal substrate
31 preference is unknown. Our cryo-electron microscopy structure of human SIRT6 in complex with
32 the nucleosome shows that the catalytic domain of SIRT6 pries DNA from the nucleosomal entry-
33 exit site and exposes the histone H3 N-terminal helix, while the SIRT6 zinc-binding domain binds
34 to the histone acidic patch using an arginine anchor. In addition, SIRT6 forms an inhibitory
35 interaction with the C-terminal tail of histone H2A. The structure provides insights into how
36 SIRT6 can deacetylate both H3 K9 and H3 K56.

37 Teaser

38 The structure of the SIRT6 deacetylase/nucleosome complex suggests how the enzyme acts on
39 both histone H3 K9 and K56 residues.

40 Introduction

41 Sirtuins are evolutionarily conserved metabolic sensor enzymes that use NAD⁺ as a coenzyme (1,
42 2). A critical role of sirtuins in aging was first suggested by studies of yeast Sir2 (3). In mammals,
43 depletion of the SIRT6 sirtuin results in shortened lifespans while SIRT6 overexpression
44 extended lifespans (4–7). Additionally, SIRT6 is associated both with tumor suppression and
45 tumorigenesis in different cancers (8). These aging and cancer-related phenotypes are linked to
46 the ability of SIRT6 to deacetylate substrates such as tumor necrosis factor- α (TNF- α) (9) and
47 to deacetylate histone H3K9ac and H3K56ac on nucleosomes (10, 11). Histone H3K9ac is a mark
48 of transcriptionally active promoters (12) and histone H3K9 acetylation plays an important role in
49 DNA repair and telomere maintenance. Crystal structures and biochemical studies have explored
50 how SIRT6 binds a peptide substrate, its NAD⁺ cofactor and allosteric effectors (9, 13–20).
51 However, the molecular basis for the sequence preference of SIRT6 to deacetylate histone H3 at
52 positions K9 and K56 (10, 21, 22) is not known. Nor do we understand the structural basis for the
53 preference of SIRT6 to deacetylate nucleosomes at H3 K9 and K56 over free histones (23). To
54 address these deficiencies, we have determined the structure of SIRT6 in complex with its
55 nucleosome substrate. The multivalent interactions between SIRT6 and both histone and DNA
56 components of the nucleosome provide insights into how SIRT6 can deacetylate exposed H3 K9
57 and occluded H3 K56 residues.

58
59
60

61 Results

62 SIRT6-nucleosome structure determination

63 We obtained 2.7 – 3.1 Å resolution cryo-EM maps of SIRT6 in complex with a 172 bp
64 nucleosome containing a 26 bp DNA extension on one end (**Fig. 1, Figs. S1 & S2**). Although our
65 sample was prepared in the presence of SNF2h, which SIRT6 recruits to sites of DNA damage
66 (24), we do not see density for SNF2h. This suggests that the ATPase may engage with either the
67 nucleosome and/or SIRT6 in a transient or flexible manner. We also do not see density for the
68 intrinsically disordered C-terminal domain of SIRT6, which was previously reported to bind
69 nucleosomal DNA (25). This does not exclude the possibility that dynamic interactions between
70 the SIRT6 C-terminal domain and nucleosomal DNA were not resolved by single particle cryo-
71 EM. Our data also yielded a subset of particles containing two copies of SIRT6 simultaneously
72 bound to opposite faces of the nucleosome (**Fig. S2**). The density for the SIRT6 bound to the face
73 associated with the DNA extension appears much stronger relative to the density for the SIRT6 on
74 the opposite face without extended DNA, suggesting that the presence of extended DNA
75 stabilizes the positioning of SIRT6 on the nucleosome.

76 Overview of SIRT6-nucleosome complex

77 Our study shows that the SIRT6 deacetylase domain forms multivalent interactions with the
78 nucleosome via the nucleosome acidic patch, the H3 N-terminal histone tail, the C-terminal H2A
79 tail and nucleosomal DNA (**Fig. 1**). The structure of SIRT6 is very similar in the absence or
80 presence of the nucleosome except for residues in and around the SIRT6 NAD⁺ binding loop and
81 separately, the 10 residues that form the SIRT6-specific extended loop in its zinc-binding domain
82 (13). The orientation of the SIRT6 zinc-binding motif with respect to its catalytic Rossmann-fold
83 domain is unchanged upon nucleosome binding. In contrast, the nucleosome is partially
84 unwrapped, with DNA displaced from the extended end of the nucleosome to accommodate
85 SIRT6-DNA interactions.

86 SIRT6-nucleosome acidic-patch interaction

87 Previous biochemical experiments indicate that SIRT6 engages with a nucleosome through the
88 acidic patch formed by histones H2A and H2B (25), and hydrogen-deuterium exchange mass
89 spectrometry experiments suggested that an N-terminal helix of SIRT6 (residues 28-43) may
90 participate in nucleosome interactions (25). However, our structure shows that SIRT6 binds to
91 the acidic patch using the extended loop (¹⁶⁷TVAKARGLRA¹⁷⁶) (**Fig. 2A**) in its zinc-binding
92 domain that is absent in other sirtuins (13). In the previous hydrogen-deuterium exchange
93 experiments (25), peptides for zinc-binding domain were not observed, which likely prevented
94 assessing whether this region interacts with the nucleosome. The zinc-binding domain can be
95 thought of as a pipe that fills the shallow ditch formed by the H2A/H2B acidic patch. These
96 contacts are mediated by a combination of hydrophilic and van der Waals interactions. Prominent
97 among these interactions is SIRT6 R175 which makes an arginine anchor interaction with H2A
98 acidic patch residues E61, D90 and E92. In addition, other SIRT6 basic residues interact with the
99 acidic patch. SIRT6 R172 constitutes a type 1 variant arginine and interacts with H2A E56, H2B
00 Q44 and E110, while SIRT6 R178 acts as an atypical arginine to interact with H2A D90 and E92
01 following the arginine-acidic patch nomenclature proposed by McGinty and Tan (26). In
02 addition, SIRT6 K170 makes ionic interactions with H2A E64. These contacts are consistent with
03 biochemical data where mutation of H2A residues E61, E64, D90, and E92 to alanines resulted in
04 weaker SIRT6 binding (25). Mutating each of these SIRT6 basic side chains (K170, R172, R175
05 and R178) to alanine reduced binding to nucleosomes (**Fig. 2B**), with R175 showing the largest
06 effect with ~9-fold weaker binding consistent with its critical role as an arginine anchor.

07 Furthermore, the SIRT6(R175A) has little or no H3K9ac nucleosomal deacetylation activity,
08 corroborating the importance of the R175 arginine anchor for SIRT6 enzymatic activity (**Fig. 2C**).

09 **SIRT6-H2A tail interaction**

10 In most nucleosome complex structures, the H2A C-terminal tail is disordered beyond K118 or
11 K119. In our SIRT6-nucleosome structure, weak density for approximately 10 more residues of
12 the histone H2A C-terminal tail is visible and tracks upwards to interact with the SIRT6 catalytic
13 domain (**Fig. 3A**). This interaction was not predicted in previous SIRT6 studies and to the best of
14 our knowledge, this is the first example of a chromatin enzyme interacting with the H2A C-
15 terminal tail. To test the importance of the H2A C-terminal tail interaction, we reconstituted
16 nucleosomes with histone H2A lacking the C-terminal tail and tested the ability of SIRT6 to
17 deacetylate H3K9ac on these nucleosomes. Intriguingly, we observe increased SIRT6 H3K9ac
18 deacetylation activity on nucleosomes lacking the H2A C-terminal tail (**Fig. 3B**). This suggests
19 that the H2A tail may have an inhibitory role in regulating SIRT6 deacetylation activity on the
20 nucleosome.

21 Our SIRT6-nucleosome sample used for structural determination lacks NAD⁺, which is a
22 necessary co-factor for SIRT6 deacetylation activity (27). In comparison to crystal structures of
23 SIRT6 bound to ADP-ribose (9, 13–20), we notice that the density for SIRT6 residues 64-80 is
24 missing in our map, although they are resolved in the crystal structures without nucleosomes (**Fig.**
25 **3A, Fig. S3**). This region of SIRT6 contains residue R65, which makes extensive contacts with
26 the adenosine ribose and pyrophosphate of ADP-ribose in solved crystal structures and is
27 important for the activation of SIRT6 for catalysis (28). The lack of defined density in our map
28 suggests that this region is flexible in the absence of a bound co-factor and only becomes
29 stabilized after co-factor binding. Previous biochemical data showing that R65 mediates a
30 necessary conformational change for activation supports this interpretation (28).

31 **SIRT6-nucleosome DNA interactions**

32 A previous prediction suggested that the disordered SIRT6 CTD can bind DNA (25). We find
33 instead that the SIRT6 catalytic domain interacts with nucleosomal DNA. We observe multiple
34 arginine residues within the SIRT6 catalytic domain (R205, R220, R231, R232, R248) that
35 contact nucleosomal DNA near the entry-exit site of the nucleosome. R205, R231 and R232
36 contact the DNA phosphate backbone at superhelical location 6 (SHL+6) while R248 binds across
37 the major groove to the opposite DNA strand phosphate backbone at SHL+7 just beyond the
38 nucleosome core (**Fig. 3C**). The polar residue, N224, in the vicinity may also have a role in the
39 interaction. These interactions are made only to the DNA phosphate backbone with no apparent
40 contacts to the nucleotide bases. To determine the contribution of these residues to SIRT6-
41 nucleosome binding, we generated three sets of SIRT6 mutants: an R205E/R231E/R232E triple
42 mutant, an R220E/N224D double mutant, and an R248E point mutant. SIRT6(R248E) binding to
43 nucleosomes was severely impaired (~12-fold weaker vs. wild-type), and the SIRT6 triple and
44 double mutants were no longer able to bind nucleosomes at all (**Fig. 3D**). These results suggest
45 that the SIRT6 globular domain interactions with nucleosomal DNA play a critical role in
46 stabilizing the SIRT6-nucleosome complex. We also generated and visualized two new SIRT6-
47 nucleosome complexes, containing shorter DNA constructs (147 and 145 bp, **Figs. S4 & S5**).
48 These reconstructions revealed significantly reduced quality of SIRT6, thereby further suggesting
49 that DNA-SIRT6 interactions play a significant role in the stabilization of the complex.

50 **Positioning of H3 substrate residues**

51 We have built H3 residues 3-12 into relatively weak density occupying the same peptide substrate
52 binding site in previous SIRT6/myristoylated H3 peptide crystal structures (9, 15). In our

53 structural model, the conformation of the H3 tail substrate is similar but not identical to the
54 SIRT6/myristoylated H3 peptide structures with the H3 K9 side chain positioned essentially
55 equivalent to the myristoylated H3 K9. The H3 tail substrate is sandwiched between the SIRT6
56 active site and nucleosomal DNA, allowing the H3 K4 side chain to fill the DNA minor groove at
57 SHL 6.5 (**Fig. 4A**). We wondered if this H3 K4-DNA interaction and potential interactions made
58 by H3 residues between K4 and K9 might account for the H3K9 histone deacetylase specificity of
59 SIRT6. We therefore assayed the histone deacetylase activity of SIRT6 on H3 K9 acetylated
60 nucleosomes also containing H3 mutated at specific tail residues. Mutating the H3 K4 to
61 glutamic acid slightly decreased the ability of SIRT6 to deacetylate H3 K9 (**Fig. 4B**) in
62 nucleosomes. Similar modest adverse effects on SIRT6 H3 K9 deacetylation were observed
63 when the H3 R8 side chain, which might interact with SIRT6, was removed and when one residue
64 between H3 K4 and K9, Q6, was deleted. These results suggest a role of H3 residues 4-8 in
65 SIRT6 deacetylation of H3 K9, but further investigation will be needed to determine what defines
66 the specificity of SIRT6 for H3 K9.

67 Although we observe H3K9 in the SIRT6 active site, H3K56 is far from SIRT6 active site (**Fig.**
68 **4C**). In agreement with previous biochemical results (23), we observe that SIRT6 deacetylates
69 H3K56ac albeit less efficiently compared to H3K9ac (**Fig. 4D, middle vs left**). Our structural
70 observation of H3K56 being distant from the SIRT6 active site raises the question of how SIRT6
71 accesses H3K56 for deacetylation (discussed further below). We further note that while a
72 previous study proposed that nucleosomal H3K27ac is also a substrate for SIRT6 (29), we find
73 that SIRT6 does not deacetylate nucleosomal H3K27ac (**Fig. 4D, right**).

74

75 Discussion

76 We have determined the cryo-EM structure of the SIRT6 histone deacetylase in complex with the
77 nucleosome. Our structure explains how SIRT6 deacetylates histone H3 K9 in its physiological
78 nucleosome substrate more efficiently than in peptide substrates. We observe that SIRT6 binds at
79 the nucleosome entry-exit site, using its globular domain to pry DNA from the histone octamer.
80 This action is facilitated by SIRT6's multivalent interactions with both histone and DNA
81 components of the nucleosome using its catalytic and zinc-binding domains which are rigidly
82 attached to each other. On one end, SIRT6 uses its zinc-binding domain to dock onto the histone
83 acidic patch. On the other end, SIRT6's catalytic domain binds to nucleosomal DNA at the entry-
84 exit site replacing contacts otherwise made by the histone H3 N-terminal helix and thus partially
85 exposing this helix. This release also allows the histone H3 N-terminal tail region to position the
86 target H3 K9 side chain into the SIRT6 catalytic site while simultaneously inserting the H3 K4
87 side chain into the nucleosome DNA minor groove at SHL 6.5. Thus, SIRT6's multiple
88 interactions with the nucleosome likely facilitates productive binding of the H3 tail for catalysis.

89 The histone dimer acidic patch is a frequent target of chromatin enzymes and factors with an
90 arginine anchor often used to bind this nucleosomal patch. SIRT6 uses R175 in the zinc-binding
91 domain as an arginine anchor to bind to the histone dimer acidic patch, with the arginine side
92 chain matching the tightly clustered conformation of arginine anchors in other chromatin
93 complexes (26). The critical importance of the R175 arginine anchor for SIRT6 function is
94 confirmed by the approximate 10-fold reduction binding affinity to nucleosomes and apparent
95 complete loss of H3 K9 deacetylase activity. We also find that mutations of SIRT6 zinc-binding
96 domain basic residues K170, R172 and R178 adversely affect nucleosome binding, consistent
97 with their interactions with the histone dimer acidic patch observed in our cryo-EM structure.

98 Unlike H3 K9 which resides in the unstructured H3 N-terminal tail, H3 K56 is located on the H3
99 N-terminal helix which interacts with nucleosomal DNA in the absence of SIRT6. It was

00 previously unclear how SIRT6 would then be able to access the H3 K56 side chain for catalysis.
01 Our structure shows that SIRT6 prying apart nucleosomal DNA from the histone octamer also
02 exposes the H3 N-terminal helix (Fig. 4C). Conversely, acetylation of H3 K56 increases
03 unwrapping of entry-exit nucleosomal DNA (30, 31). In our structure, the alpha carbons of
04 H3K56 and H3K9 are 25 Å apart and it is clear that in this state H3 K56 cannot reach the SIRT6
05 active site. We propose that the conformational flexibility in the 10 residue insertion of the
06 SIRT6 zinc-finger domain might allow SIRT6 to pivot as a rigid body about the histone acidic
07 patch to approach the histone core. This and the possible unwinding of the H3 N-terminal helix
08 might allow H3K56 to enter the SIRT6 catalytic site. The additional distortions necessary for this
09 to occur could explain the lower deacetylase activity on H3K56 substrates.

10 The H2A C-terminal tail interacts with a SIRT6 short helix adjacent to both the SIRT6 NAD⁺
11 binding loop (residues 55-65) and the allosteric binding pocket targeted by both activators MDL-
12 801 and quercetin activators and the catechin gallate inhibitor (Fig. 3A). For this reason and our
13 observation of the inhibitory effect of the SIRT6-H2A tail interaction, we suspect that this
14 structure represents SIRT6 bound to a nucleosome in an inhibited, non-activated state. Since the
15 unbound structure of SIRT6 is largely unchanged when activated or inhibited by the allosteric
16 effectors, it is possible or even likely that activation of SIRT6 will involve local conformational
17 changes near the catalytic site without major changes in how SIRT6 binds to the nucleosome via
18 interactions with the histone acidic patch or nucleosomal DNA. This underscores the significance
19 of the SIRT6 allosteric binding pocket as a target for drug discovery as well as the importance of
20 using physiological nucleosome substrates for characterizing the effect of drug candidates on the
21 enzymatic activity of SIRT6.

22 Our structural and biochemical studies explain how multivalent interactions of SIRT6 with both
23 histone and DNA components of the nucleosome enable SIRT6 to deacetylate H3K9ac. It should
24 be noted that the SIRT6-nucleosome used for our structural studies did not include NAD⁺ or a
25 cofactor analog. We suspect this is not a serious limitation since the SIRT6 catalytic domain
26 adopts the same structure in the presence or absence of cofactor (13, 32). In terms of substrate
27 specificity, our structure suggested possible mechanistic roles for specific H3 residue side-chains
28 N-terminal to the H3 K9 target residue. However, the modest effect of mutating these residues on
29 the H3K9ac deacetylase activity of SIRT6 suggests either a concerted role for these N-terminal
30 residues or a more complicated explanation for why SIRT6 targets H3 K9 versus other lysines
31 present in the unstructured H3 tail. The relatively weak density for the H3 tail peptide also limits
32 our confidence in the quality of the structure in this particular region. Our SIRT6-nucleosome
33 atomic model provides the structural framework for further studies to understand H3K9
34 specificity and remaining issues such how SIRT6 engages H3K56 for deacetylation and the role
35 of the H2A tail in SIRT6 function.

36

Materials and Methods

Nucleosome preparation

Three DNA constructs centered on the Widom 601 sequence (33) were used for nucleosome assembly; these constructs consisted of 145 (0-145-0), 147 (1-145-1), and 172 (1-145-26) base pairs of DNA. Recombinant H3 and H4 *Xenopus laevis* histones and H2A and H2B human histones were expressed, purified, and reconstituted with each DNA construct as described previously (34), including anion-exchange purification of the nucleosomes.

Protein purification

The gene coding for the full-length human SIRT6 (UniProtKB: Q8N6T7) was cloned into pST50Tr (35) vector with an N-terminal GSS-hexahistidine (His₆). GSS-(His₆)-SIRT6 was expressed in BL21(DE3) pLysS *Escherichia coli* cells at 23°C. Bacterial cells were lysed by sonication, and the crude lysate centrifuged at 36,000 g for 40 min at 4°C. The protein was purified by metal-affinity chromatography (Talon resin, Clontech), the affinity tag removed using tobacco etch virus (TEV) protease and the protein further purified by Source S cation-exchange chromatography (Cytiva).

His₆-tagged human SNF2h was expressed and purified as previously described with minor modifications (36). Briefly, His₆-SNF2h was expressed in BL21(DE3) Rosetta *Escherichia coli* cells at 18°C. Cells were lysed via sonication, and Ni-NTA affinity chromatography used to isolate His₆-SNF2h from the clarified lysate. TEV protease was used to remove the His₆-tag, and the untagged SNF2h was passed through a HiTrapQ column (Cytiva) to remove contaminating DNA. The protein was then run over a HiLoad Superdex200 column (Cytiva), and pure fractions were pooled, aliquoted, and stored at -80 °C.

Cryo-EM sample preparation

SIRT6 was reconstituted in reconstitution buffer (20 mM HEPES pH 7.5, 75 mM NaCl, 1 mM DTT) at 0.8:1 enzyme:nucleosome ratio with the 145 and 147 base pair nucleosomes, and at 2.2:1 ratio with the 172 base pair nucleosomes. SNF2h was also included in the SIRT6-172 base pair nucleosome sample at 1.1-fold excess over nucleosome.

The SIRT6-147 base pair nucleosome sample was crosslinked in reconstitution buffer with 0.05% glutaraldehyde. The sample was incubated on ice for 10 minutes and then quenched with 100 mM Tris-HCl pH 7.5. The SIRT6-145 base pair / SIRT6-172 base pair nucleosome samples were first purified using a Superdex 200 column (GE Healthcare) and then stabilized using the GraFix method (37). Light buffer (20 mM HEPES pH 7.5, 75 mM NaCl, 1 mM DTT, 10% glycerol) and heavy buffer (20 mM HEPES pH 7.5, 75 mM NaCl, 1 mM DTT, 40% glycerol, 0.15% glutaraldehyde) were used to generate a 10-40% glycerol gradient with a 0-0.15% glutaraldehyde gradient. Fractions from the gradient were checked via native PAGE. Fractions containing the SIRT6-nucleosome complex were concentrated and buffer exchanged into EM buffer (12.5 mM HEPES pH 7.5, 60 mM KCl, 1.5% glycerol, 1 mM DTT for SIRT6-172 base pair nucleosome and 20 mM HEPES pH 7.5, 75 mM NaCl, 1 mM DTT for SIRT6-145 base pair nucleosome). The final concentration of the SIRT6-nucleosome samples was ~3 μM.

Cryo-EM grids of the complexes were prepared using an established procedure (38). Specifically, 3.5 μL of the concentrated sample was applied to copper Quantifoil 2/2 Cu200 (172 base pair sample) or 1.2/1.3 Cu300 (145/147 base pair samples) mesh grids in a FEI Vitrobot Mark IV maintained at 4°C with 100% humidity. The sample was blotted for 3.5 s with a blot force of -1 and then plunge-frozen into liquid ethane.

Cryo-EM data collection

86 The SIRT6-147 base pair nucleosome dataset was collected at the Penn State Cryo-Electron
87 Microscopy Facility on a Titan Krios operated at 300 keV and equipped with an FEI Falcon 3
88 direct electron detector operated in counting mode. 524 movies were collected at 59,000x
89 magnification, which corresponds to 1.14 Å/pixel, at a defocus range of -0.5 to -2.5 μm with ~58
90 e/Å² accumulated exposure divided between 44 frames (Table S1).

91 The SIRT6-145 base pair nucleosome dataset was collected at the Pacific Northwest Cryo-
92 EM Center on a Titan Krios operated at 300 keV and equipped with a Gatan K3 direct electron
93 detector and an energy filter (20 eV slit). 7,730 movies were collected in counting mode at
94 81,000x magnification, which corresponds to 1.059 Å/pixel, at a defocus range of -0.8 to -2.2 μm
95 with ~50 e/Å² accumulated exposure divided between 44 frames (Table S1).

96 The SIRT6-172 base pair nucleosome dataset was collected at the National Cancer Institute
97 using a Titan Krios operated at 300 keV and equipped with a Gatan K3 direct electron detector
98 and an energy filter (20 eV slit). The data was collected over the course of two separate sessions
99 at 81,000x magnification, which corresponds to 1.08 Å/pixel (0.54 Å/pixel in Super-Resolution
00 mode), at a defocus range of -1.0 to -2.2 μm with ~50 e/Å² accumulated exposure fractionated
01 into 40 super-resolution frames. In total, 11,872 movies were collected over the two sessions
02 (5,122 movies in the first session and 6,750 movies in the second session; Table S1).

03 04 **Cryo-EM data processing**

05 The SIRT6-172 base pair nucleosome dataset was imported into RELION v3.1 (39, 40).
06 Using UCSF MotionCor2 v1.4.1 (41) within RELION, raw movies were motion-corrected,
07 binned 2x to 1.08 Å/pixel, and the resulting dose-weighted micrographs (42) were imported into
08 cryoSPARC (43). *Patch CTF estimation (multi)* was used to estimate defocus values. A
09 nucleosome map was used to generate templates for template picking of particles; these particles
10 were then extracted using a 300 pixel box Fourier-binned to 100 pixels (resulting in 3.24 Å/pixel).
11 2D classification was performed and classes containing obvious junk were removed. Ab-initio
12 reconstruction was performed with the remaining particles to generate input classes for
13 heterogeneous refinement. Subsequently, a cleaned dataset of nucleosomal ~~the~~ particles was
14 subjected to numerous rounds of 3D classification, yielding a single class with a strong density
15 for SIRT6. To further the quality of the complex, 3D classification without alignment in
16 RELION was performed with a mask focused on the globular domain of SIRT6 and the adjacent
17 DNA. A class with 71,603 particles that represented the most stable positioning of SIRT6 on the
18 nucleosome visually was selected. These particles were refined using non-uniform refinement
19 (44) in cryoSPARC, as well as with RELION and with cisTEM (45). All reconstructions looked
20 reasonable, but the cisTEM reconstruction was used for further interpretation.

21 Subsequently, Bayesian polishing was performed in RELION to further improve the quality
22 of the map (46). Two rounds of Bayesian polishing and CTF refinement were performed using
23 1,007,638 particles from an earlier 2.83 Å consensus reconstruction. This improved the resolution
24 of the consensus reconstruction to 2.63 Å. Using these optimized particles, the 71,603-particle
25 subset was refined to 3.07 Å with improved quality of SIRT6 (Figs. S1 & S2; Table S1).

26 The 147 base pair dataset containing 524 movies was first motion-corrected using
27 cryoSPARC's *Patch motion correction (multi)*. Defocus values were calculated using *Patch CTF*
28 *estimation (multi)*, and 398,186 particles were blob picked using a sphere with a radius of 120-
29 140 Å and extracted in a 256 pixel box. Five models were generated using ab initio reconstruction
30 and the particles were subjected to heterogeneous refinement. One class was selected based on the
31 presence of SIRT6 and refined to 4.84 Å using non-uniform refinement. These particles were then
32 subjected to classification with the best reconstruction from the previous step seeded three times.
33 One of the resulting maps exhibited a more stable SIRT6-nucleosome complex and was subjected
34 to non-uniform refinement that yielded a reconstruction at 5.0 Å. Using these particles, we re-

35 extracted the subset in a larger 300 pixel box; this yielded 40,834 particles that we refined the 4.9
36 Å final resolution using *Non-Uniform Refinement (New)* (Fig. S4; Table S1).

37 The SIRT6-145 bp nucleosome dataset was processed as described for SIRT6-
38 147 bp nucleosome datasets, except for motion correction – here, we used UCSF MotionCor2
39 instead. We obtained two final reconstructions, differing in their SIRT6-interacting DNA: a) 3.28
40 Å reconstruction from 31,802 particles (Fig S5C-E, I; Table S1) and b) 3.27Å reconstruction from
41 34,737 particles (Fig S5F-H,J; Table S1).

42 The final resolutions reported were calculated using Fourier Shell Correlation (FSC) and
43 assessed at the 0.143 cutoff following gold-standard refinement (47). All file format conversions
44 between cryoSPARC and RELION, as well as particle stack preparation for cisTEM refinement
45 were performed using UCSF pyem v0.5 (48).

46 47 **Model building and refinement**

48 PDB 3LZ0 (49) was used as a starting model for the nucleosome, and 3PKI (13) and 7CL0
49 (19) were used as starting models for SIRT6. The models were rigid-body fitted into the 3.07 Å
50 reconstruction using the “fit in map” function in UCSF ChimeraX (50) and then further optimized
51 in Coot (51).

52 A combination of 3D Coulomb potential maps from the 172 base pair dataset were used to
53 construct the final model. Using the highest resolved 2.63 Å reconstruction in Coot, histones and
54 core DNA were optimized and the SIRT6 acidic patch-interacting loop was constructed. The 3.07
55 Å reconstruction was then used to position and adjust the SIRT6 globular domain, zinc-binding
56 domain, histone H2A C-terminal tail, histone H3 N-terminal tail, and the DNA overhang. The
57 final model was refined using phenix.real_space_refine (52) with secondary structure,
58 Ramachandran, and rotamer restraints. Lastly, the model was validated manually in Coot and with
59 Molprobity (53) using comprehensive validation (cryo-EM) in Phenix. Model statistics are
60 reported in Table S2.

61 62 **Electrophoresis Mobility Shift Assays (Nucleosome Binding Assays)**

63 10 µL reactions of SIRT6 variants at indicated concentrations were incubated with 100 nM
64 of wild-type NCPs for 30 min at 30°C in 5x binding buffer (25 mM HEPES pH 7.3, 150 mM
65 NaCl, 4.5 mM MgCl₂, 1 mM DTT, 0.01% Tween, 0.1 mg/ml BSA). Reactions were quenched
66 with 2 µL of 50% glycerol and electrophoresed on 4.5% native PAGE gels at 100 V, 4 °C.

67 68 **Histone Deacetylation Assays**

69 Wild-type SIRT6 (500nM or 125nM) and SIRT6(R175A) (200nM) was incubated with
70 nucleosomes (125nM) containing either acetylated H3K9, H3K56, or H3K27, and/or with
71 truncated H2A (H2At) at 37 °C for varying time points in HDAC reaction buffer (25mM HEPES
72 pH 7.3, 49 mM NaCl, 4.5mM MgCl₂, 1mM DTT). Reactions were quenched with the addition of
73 2X SDS sample buffer, boiled, and then electrophoresed on a 12 % SDS-PAGE gel. Proteins on
74 the gel were transferred to a PVDF membrane (Millipore IPFL 00010), which was first blocked
75 with 10 % milk, and then probed with either 1:10,000 anti-H3K9ac antibody (Active Motif
76 #39038), 1:1,000 anti-H3K56ac antibody (Active Motif #39133), or 1:3,000 anti-H3K27ac
77 antibody (Active Motif #39082), and also probed with 1:3,000 anti-H2B antibody (Abcam
78 #64039). Western blots were quantified using ImageJ (54) or Bio-Rad Image Lab.

79

80

81

- 82 1. R. H. Houtkooper, E. Pirinen, J. Auwerx, Sirtuins as regulators of metabolism and healthspan. *Nat. Rev. Mol.*
83 *Cell Biol.* **13**, 225–238 (2012).
- 84 2. Z. Mei, X. Zhang, J. Yi, J. Huang, J. He, Y. Tao, Sirtuins in metabolism, DNA repair and cancer. *J. Exp. Clin.*
85 *Cancer Res.* **35**, 182 (2016).
- 86 3. M. Kaeberlein, M. McVey, L. Guarente, The SIR2/3/4 complex and SIR2 alone promote longevity in
87 *Saccharomyces cerevisiae* by two different mechanisms. *Genes Dev.* **13**, 2570–2580 (1999).
- 88 4. R. Mostoslavsky, K. F. Chua, D. B. Lombard, W. W. Pang, M. R. Fischer, L. Gellon, P. Liu, G. Mostoslavsky,
89 S. Franco, M. M. Murphy, K. D. Mills, P. Patel, J. T. Hsu, A. L. Hong, E. Ford, H. L. Cheng, C. Kennedy, N.
90 Nunez, R. Bronson, D. Frendewey, W. Auerbach, D. Valenzuela, M. Karow, M. O. Hottiger, S. Hursting, J. C.
91 Barrett, L. Guarente, R. Mulligan, B. Demple, G. D. Yancopoulos, F. W. Alt, Genomic instability and aging-
92 like phenotype in the absence of mammalian SIRT6. *Cell.* **124**, 315–329 (2006).
- 93 5. Y. Kanfi, S. Naiman, G. Amir, V. Peshti, G. Zinman, L. Nahum, Z. Bar-Joseph, H. Y. Cohen, The sirtuin
94 SIRT6 regulates lifespan in male mice. *Nature.* **483**, 218–221 (2012).
- 95 6. A. Roichman, S. Elhanati, M. A. Aon, I. Abramovich, A. Di Francesco, Y. Shahar, M. Y. Avivi, M. Shurgi, A.
96 Rubinstein, Y. Wiesner, A. Shuchami, Z. Petrover, I. Lebenthal-Loinger, O. Yaron, A. Lyashkov, C. Ubaida-
97 Mohien, Y. Kanfi, B. Lerrer, P. J. Fernández-Marcos, M. Serrano, E. Gottlieb, R. de Cabo, H. Y. Cohen,
98 Restoration of energy homeostasis by SIRT6 extends healthy lifespan. *Nat. Commun.* **12** (2021),
99 doi:10.1038/s41467-021-23545-7.
- 00 7. J. R. Taylor, J. G. Wood, E. Mizerak, S. Hinthorn, J. Liu, M. Finn, S. Gordon, L. Zingas, C. Chang, M. A.
01 Klein, J. M. Denu, V. Gorbunova, A. Seluanov, J. D. Boeke, J. M. Sedivy, S. L. Helfand, Sirt6 regulates
02 lifespan in *Drosophila melanogaster*. *Proc. Natl. Acad. Sci. U. S. A.* **119**, 1–9 (2022).
- 03 8. V. Desantis, A. Lamanuzzi, A. Vacca, The role of SIRT6 in tumors. *Haematologica.* **103**, 1–4 (2018).
- 04 9. H. Jiang, S. Khan, Y. Wang, G. Charron, B. He, C. Sebastian, J. Du, R. Kim, E. Ge, R. Mostoslavsky, H. C.
05 Hang, Q. Hao, H. Lin, SIRT6 regulates TNF- α secretion through hydrolysis of long-chain fatty acyl lysine.
06 *Nature.* **496**, 110–113 (2013).
- 07 10. E. Michishita, R. A. McCord, E. Berber, M. Kioi, H. Padilla-Nash, M. Damian, P. Cheung, R. Kusumoto, T. L.
08 A. Kawahara, J. C. Barrett, H. Y. Chang, V. A. Bohr, T. Ried, O. Gozani, K. F. Chua, SIRT6 is a histone H3
09 lysine 9 deacetylase that modulates telomeric chromatin. *Nature.* **452**, 492–496 (2008).
- 10 11. S. Kugel, J. L. Feldman, M. A. Klein, D. M. Silberman, C. Sebastián, C. Mermel, S. Dobersch, A. R. Clark, G.
11 Getz, J. M. Denu, R. Mostoslavsky, Identification of and Molecular Basis for SIRT6 Loss-of-Function Point
12 Mutations in Cancer. *Cell Rep.* **13**, 479–488 (2015).
- 13 12. K. Karmodiya, A. R. Krebs, M. Oulad-Abdelghani, H. Kimura, L. Tora, H3K9 and H3K14 acetylation co-
14 occur at many gene regulatory elements, while H3K14ac marks a subset of inactive inducible promoters in
15 mouse embryonic stem cells. *BMC Genomics.* **13**, 424 (2012).
- 16 13. P. W. Pan, J. L. Feldman, M. K. Devries, A. Dong, A. M. Edwards, J. M. Denu, Structure and biochemical
17 functions of SIRT6. *J. Biol. Chem.* **286**, 14575–14587 (2011).
- 18 14. W. You, D. Rotili, T. M. Li, C. Kambach, M. Meleshin, M. Schutkowski, K. F. Chua, A. Mai, C. Steegborn,
19 Structural Basis of Sirtuin 6 Activation by Synthetic Small Molecules. *Angew. Chem. - Int. Ed.* **56**, 1007–1011
20 (2017).
- 21 15. Z. Huang, J. Zhao, W. Deng, Y. Chen, J. Shang, K. Song, L. Zhang, C. Wang, S. Lu, X. Yang, B. He, J. Min,
22 H. Hu, M. Tan, J. Xu, Q. Zhang, J. Zhong, X. Sun, Z. Mao, H. Lin, M. Xiao, Y. E. Chin, H. Jiang, Y. Xu, G.
23 Chen, J. Zhang, Identification of a cellularly active SIRT6 allosteric activator. *Nat. Chem. Biol.* **14**, 1118–1126
24 (2018).
- 25 16. W. You, C. Steegborn, Structural Basis of Sirtuin 6 Inhibition by the Hydroxamate Trichostatin A:
26 Implications for Protein Deacetylase Drug Development. *J. Med. Chem.* **61**, 10922–10928 (2018).

- 27 17. W. You, C. Steegborn, Structural Basis for Activation of Human Sirtuin 6 by Fluvastatin. *ACS Med. Chem.*
28 *Lett.* **11**, 2285–2289 (2020).
- 29 18. W. You, C. Steegborn, Binding site for activator MDL-801 on SIRT6. *Nat. Chem. Biol.* **17**, 519–521 (2021).
- 30 19. Z. Huang, J. Zhao, W. Deng, Y. Chen, J. Shang, K. Song, L. Zhang, C. Wang, S. Lu, X. Yang, B. He, J. Min,
31 H. Hu, M. Tan, J. Xu, Q. Zhang, J. Zhong, X. Sun, Z. Mao, H. Lin, M. Xiao, Y. E. Chin, H. Jiang, H. Shen, Y.
32 Xu, G. Chen, J. Zhang, Reply to: Binding site for MDL-801 on SIRT6. *Nat. Chem. Biol.* **17**, 522–523 (2021).
- 33 20. W. You, W. Zheng, S. Weiss, K. F. Chua, C. Steegborn, Structural basis for the activation and inhibition of
34 Sirtuin 6 by quercetin and its derivatives. *Sci. Rep.* **9**, 1–11 (2019).
- 35 21. E. Michishita, R. A. McCord, L. D. Boxer, M. F. Barber, T. Hong, O. Gozani, K. F. Chua, Cell cycle-
36 dependent deacetylation of telomeric histone H3 lysine K56 by human SIRT6. *Cell Cycle Georget. Tex.* **8**,
37 2664–2666 (2009).
- 38 22. L. Tasselli, Y. Xi, W. Zheng, R. I. Tennen, Z. Odrowaz, F. Simeoni, W. Li, K. F. Chua, SIRT6 deacetylates
39 H3K18ac at pericentric chromatin to prevent mitotic errors and cellular senescence. *Nat. Struct. Mol. Biol.* **23**,
40 434–440 (2016).
- 41 23. R. Gil, S. Barth, Y. Kanfi, H. Y. Cohen, SIRT6 exhibits nucleosome-dependent deacetylase activity. *Nucleic*
42 *Acids Res.* **41**, 8537–8545 (2013).
- 43 24. D. Toiber, F. Erdel, K. Bouazoune, D. M. Silberman, L. Zhong, P. Mulligan, C. Sebastian, C. Cosentino, B.
44 Martinez-Pastor, S. Giacosa, A. D'Urso, A. M. Näär, R. Kingston, K. Rippe, R. Mostoslavsky, SIRT6 recruits
45 SNF2H to DNA break sites, preventing genomic instability through chromatin remodeling. *Mol. Cell.* **51**, 454–
46 468 (2013).
- 47 25. W. H. Liu, J. Zheng, J. L. Feldman, M. A. Klein, V. I. Kuznetsov, C. L. Peterson, P. R. Griffin, J. M. Denu,
48 Multivalent interactions drive nucleosome binding and efficient chromatin deacetylation by SIRT6. *Nat.*
49 *Commun.* **11** (2020), doi:10.1038/s41467-020-19018-y.
- 50 26. R. K. McGinty, S. Tan, Principles of nucleosome recognition by chromatin factors and enzymes. *Curr. Opin.*
51 *Struct. Biol.* **71**, 16–26 (2021).
- 52 27. E. Michishita, R. A. McCord, E. Berber, M. Kioi, H. Padilla-Nash, M. Damian, P. Cheung, R. Kusumoto, T. L.
53 A. Kawahara, J. C. Barrett, H. Y. Chang, V. A. Bohr, T. Ried, O. Gozani, K. F. Chua, SIRT6 is a histone H3
54 lysine 9 deacetylase that modulates telomeric chromatin. *Nature.* **452**, 492–496 (2008).
- 55 28. M. A. Klein, J. M. Denu, Biological and catalytic functions of sirtuin 6 as targets for small-molecule
56 modulators. *J. Biol. Chem.* **295**, 11021–11041 (2020).
- 57 29. W. W. Wang, Y. Zeng, B. Wu, A. Deiters, W. R. Liu, A Chemical Biology Approach to Reveal Sirt6-targeted
58 Histone H3 Sites in Nucleosomes. *ACS Chem. Biol.* **11**, 1973–1981 (2016).
- 59 30. H. Neumann, S. M. Hancock, R. Buning, A. Routh, L. Chapman, J. Somers, T. Owen-Hughes, J. van Noort, D.
60 Rhodes, J. W. Chin, A method for genetically installing site-specific acetylation in recombinant histones
61 defines the effects of H3 K56 acetylation. *Mol. Cell.* **36**, 153–163 (2009).
- 62 31. J. C. Shimko, J. A. North, A. N. Bruns, M. G. Poirier, J. J. Ottesen, Preparation of Fully Synthetic Histone H3
63 Reveals That Acetyl-Lysine 56 Facilitates Protein Binding Within Nucleosomes. *J. Mol. Biol.* **408**, 187–204
64 (2011).
- 65 32. J. Zhang, Z. Huang, K. Song, Sirt6 apo structure (2017), (available at 10.2210/pdb5X16/pdb).
- 66 33. P. T. Lowary, J. Widom, New DNA sequence rules for high affinity binding to histone octamer and sequence-
67 directed nucleosome positioning. *J. Mol. Biol.* (1998), doi:10.1006/jmbi.1997.1494.
- 68 34. K. Luger, T. J. Rechsteiner, T. J. Richmond, "Preparation of Nucleosome Core Particle from Recombinant
69 Histones" in *Methods in Enzymology* (1999), vol. 304, pp. 3–19.

- 70 35. S. Tan, R. C. Kern, W. Selleck, The pST44 polycistronic expression system for producing protein complexes in
71 Escherichia coli. *Protein Expr. Purif.* **40**, 385–395 (2005).
- 72 36. J. D. Leonard, G. J. Narlikar, A Nucleotide-Driven Switch Regulates Flanking DNA Length Sensing by a
73 Dimeric Chromatin Remodeler. *Mol. Cell.* **57**, 850–859 (2015).
- 74 37. B. Kastner, N. Fischer, M. M. Golas, B. Sander, P. Dube, D. Boehringer, K. Hartmuth, J. Deckert, F. Hauer, E.
75 Wolf, H. Uchtenhagen, H. Urlaub, F. Herzog, J. M. Peters, D. Poerschke, R. Lührmann, H. Stark, GraFix:
76 Sample preparation for single-particle electron cryomicroscopy. *Nat. Methods.* **5**, 53–55 (2008).
- 77 38. X. Li, P. Mooney, S. Zheng, C. R. Booth, M. B. Braunfeld, S. Gubbens, D. A. Agard, Y. Cheng, Electron
78 counting and beam-induced motion correction enable near-atomic-resolution single-particle cryo-EM. *Nat.*
79 *Methods.* **10**, 584–590 (2013).
- 80 39. S. H. W. Scheres, RELION: Implementation of a Bayesian approach to cryo-EM structure determination. *J.*
81 *Struct. Biol.* **180**, 519–530 (2012).
- 82 40. J. Zivanov, T. Nakane, B. O. Forsberg, D. Kimanius, W. J. H. Hagen, E. Lindahl, S. H. W. Scheres, New tools
83 for automated high-resolution cryo-EM structure determination in RELION-3. *eLife.* **7**, 1–22 (2018).
- 84 41. S. Q. Zheng, E. Palovcak, J. P. Armache, K. A. Verba, Y. Cheng, D. A. Agard, MotionCor2: Anisotropic
85 correction of beam-induced motion for improved cryo-electron microscopy. *Nat. Methods.* **14**, 331–332 (2017).
- 86 42. T. Grant, N. Grigorieff, Measuring the optimal exposure for single particle cryo-EM using a 2.6 Å
87 reconstruction of rotavirus VP6. *eLife.* **4** (2015), doi:10.7554/eLife.06980.
- 88 43. A. Punjani, J. L. Rubinstein, D. J. Fleet, M. A. Brubaker, CryoSPARC: Algorithms for rapid unsupervised
89 cryo-EM structure determination. *Nat. Methods.* **14**, 290–296 (2017).
- 90 44. A. Punjani, H. Zhang, D. J. Fleet, Non-uniform refinement: adaptive regularization improves single-particle
91 cryo-EM reconstruction. *Nat. Methods.* **17**, 1214–1221 (2020).
- 92 45. T. Grant, A. Rohou, N. Grigorieff, cisTEM, user-friendly software for single-particle image processing. *eLife*
93 (2018).
- 94 46. J. Zivanov, T. Nakane, S. H. W. Scheres, A Bayesian approach to beam-induced motion correction in cryo-EM
95 single-particle analysis. *IUCrJ.* **6**, 5–17 (2019).
- 96 47. P. B. Rosenthal, R. Henderson, Optimal determination of particle orientation, absolute hand, and contrast loss
97 in single-particle electron cryomicroscopy. *J. Mol. Biol.* **333**, 721–745 (2003).
- 98 48. D. Asarnow, E. J. Palovcak, Y. Cheng, asarnow/pyem: UCSF pyem v0.5. *Zenodo* (2019).
- 99 49. D. Vasudevan, E. Y. D. Chua, C. A. Davey, Crystal Structures of Nucleosome Core Particles Containing the
00 “601” Strong Positioning Sequence. *J. Mol. Biol.* **403**, 1–10 (2010).
- 01 50. E. F. Pettersen, T. D. Goddard, C. C. Huang, E. C. Meng, G. S. Couch, T. I. Croll, J. H. Morris, T. E. Ferrin,
02 UCSF ChimeraX: Structure visualization for researchers, educators, and developers. *Protein Sci.* **30**, 70–82
03 (2021).
- 04 51. P. Emsley, B. Lohkamp, W. G. Scott, K. Cowtan, Features and development of Coot. *Acta Crystallogr. D Biol.*
05 *Crystallogr.* **66**, 486–501 (2010).
- 06 52. P. V. Afonine, B. K. Poon, R. J. Read, O. V. Sobolev, T. C. Terwilliger, A. Urzhumtsev, P. D. Adams, Real-
07 space refinement in PHENIX for cryo-EM and crystallography. *Acta Crystallogr. Sect. Struct. Biol.* **74**, 531–
08 544 (2018).
- 09 53. C. J. Williams, J. J. Headd, N. W. Moriarty, M. G. Prisant, L. L. Videau, L. N. Deis, V. Verma, D. A. Keedy,
10 B. J. Hintze, V. B. Chen, S. Jain, S. M. Lewis, W. B. Arendall, J. Snoeyink, P. D. Adams, S. C. Lovell, J. S.

- 11 Richardson, D. C. Richardson, MolProbity: More and better reference data for improved all-atom structure
12 validation. *Protein Sci.* **27**, 293–315 (2018).
- 13 54. C. A. Schneider, W. S. Rasband, K. W. Eliceiri, NIH Image to ImageJ: 25 years of image analysis. *Nat.*
14 *Methods.* **9**, 671–675 (2012).

15

16 Acknowledgments:

17 We thank Szu-Yu Kuan and Eric Baron at Penn State for nucleosome preparations, Adam Wier at
18 NCI, Theo Humphreys at PNCC for assistance with EM data collection, Joseph Cho and Carol
19 Bator of the Penn State Cryo-Electron Microscopy Facility for assistance with EM screening and
20 data collection, and Jennifer Gray at Penn State for assistance with training on the T20 for negative
21 stain EM. This work was supported by:

22 National Institutes of Health grant F32GM137463 (USC)

23 National Institutes of Health grant T32BM107000 (ARB)

24 National Institutes of Health grant R35GM122519 (CLP)

25 National Institutes of Health grant R35GM127034 (ST)

26 This project is funded, in part, under a grant from the Pennsylvania Department of Health using
27 Tobacco CURE Funds. The Department specifically disclaims responsibility for any analyses,
28 interpretations or conclusion.

29 The figures for this manuscript were generated using PyMOL and UCSF ChimeraX. UCSF
30 ChimeraX is developed by the Resource for Biocomputing, Visualization, and Informatics at the
31 University of California, San Francisco, with support from National Institutes of Health R01-
32 GM129325 and the Office of Cyber Infrastructure and Computational Biology, National Institute
33 of Allergy and Infectious Diseases.

34 Author contributions

35 Conceptualization: CLP, ST, JPA

36 Methodology: USC, OR, AB, JZ, JLF, CLP, ST, JPA

37 Investigation: USC, OR, AB, JZ, JLF, JPA

38 Visualization: ST, JPA

39 Funding acquisition: USC, CLP, ST, JPA

40 Project administration: CLP, ST, JPA

41 Supervision: CLP, ST, JPA

42 Writing – original draft: USC, ST, JPA

43 Writing – review & editing: OR, AB, CLP, ST, JPA

44

45 Competing interests

46 Authors declare that they have no competing interests.

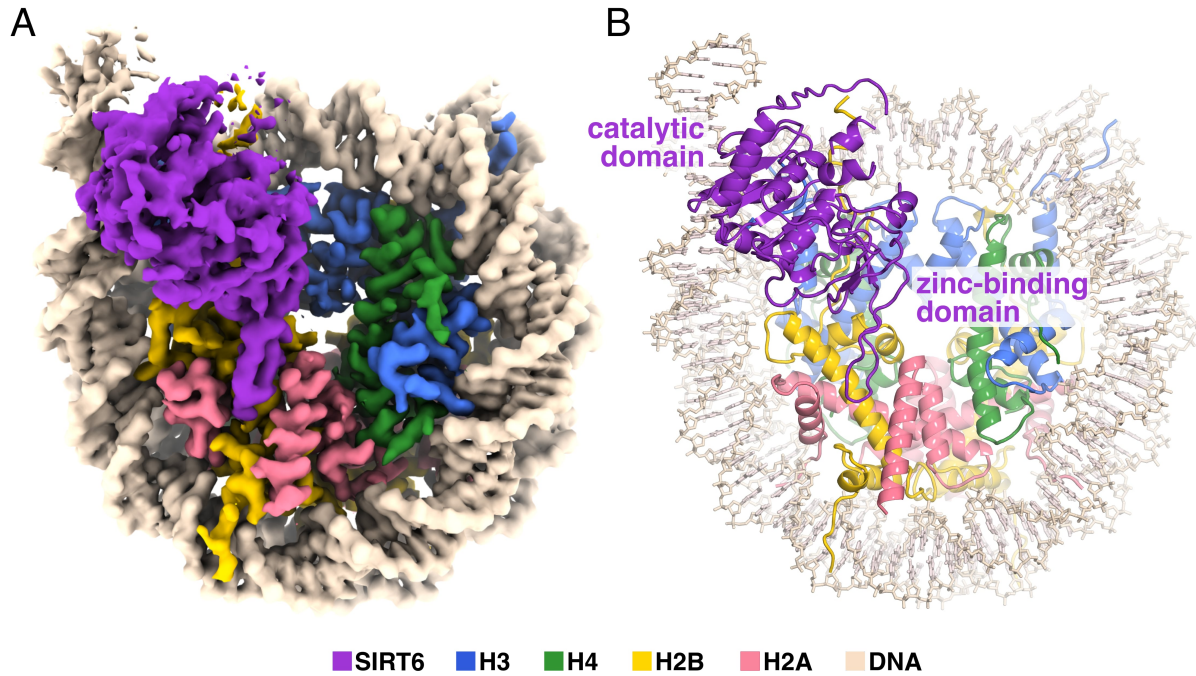
47 Data and materials availability

48
49 The atomic coordinates of the SIRT6-nucleosome complex have been deposited to the RCSB
50 Protein Data Bank with PDB ID XXXX. The cryo-EM Coulomb potential maps were deposited in
51 the Electron Microscopy Data Bank as EMD-XXXXXX (best-resolved SIRT6-nucleosome
52 complex), EMD-XXXXXY (SIRT6 in position 2), EMD-XXXXYX (SIRT6 in position 3). The raw
53 cryo-EM data was deposited in EMPIAR (EMPIAR-ZZZ).

54
55
56

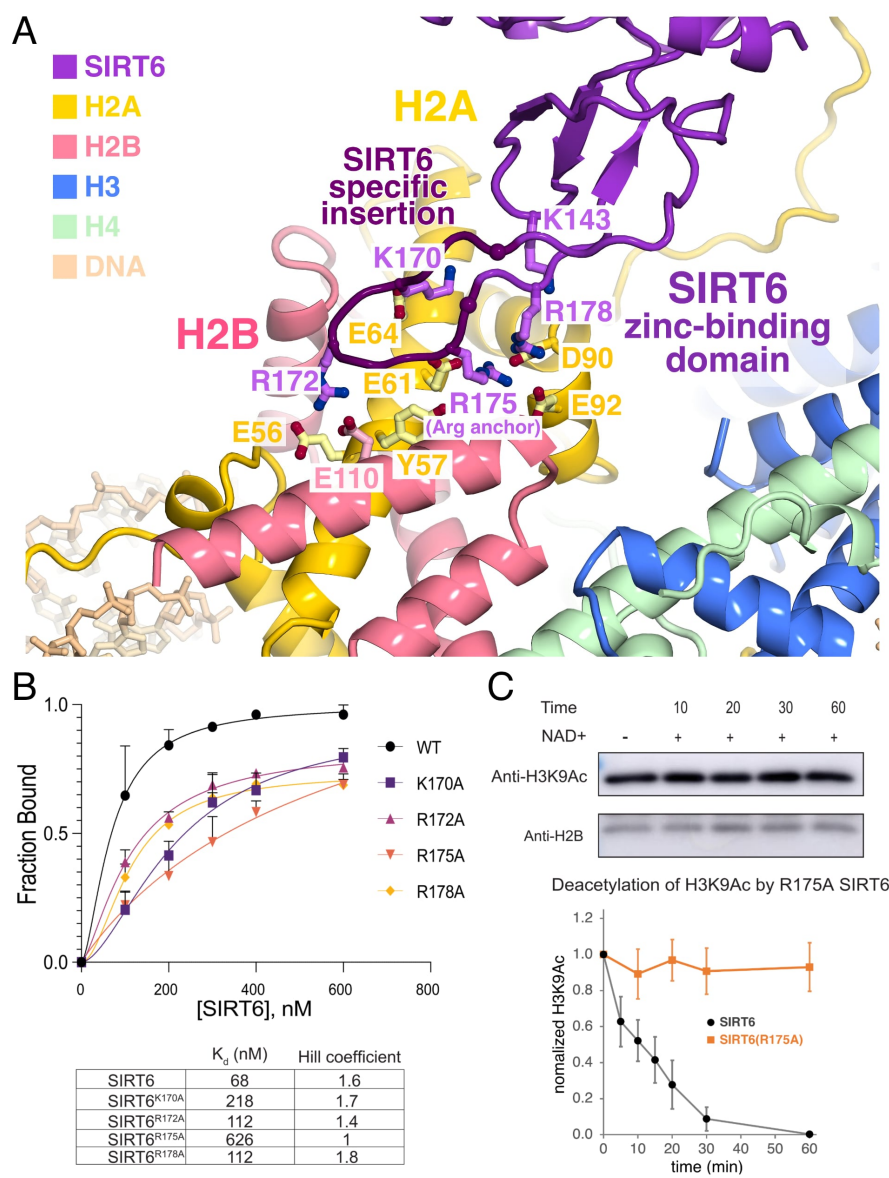
57 **Figures**

58



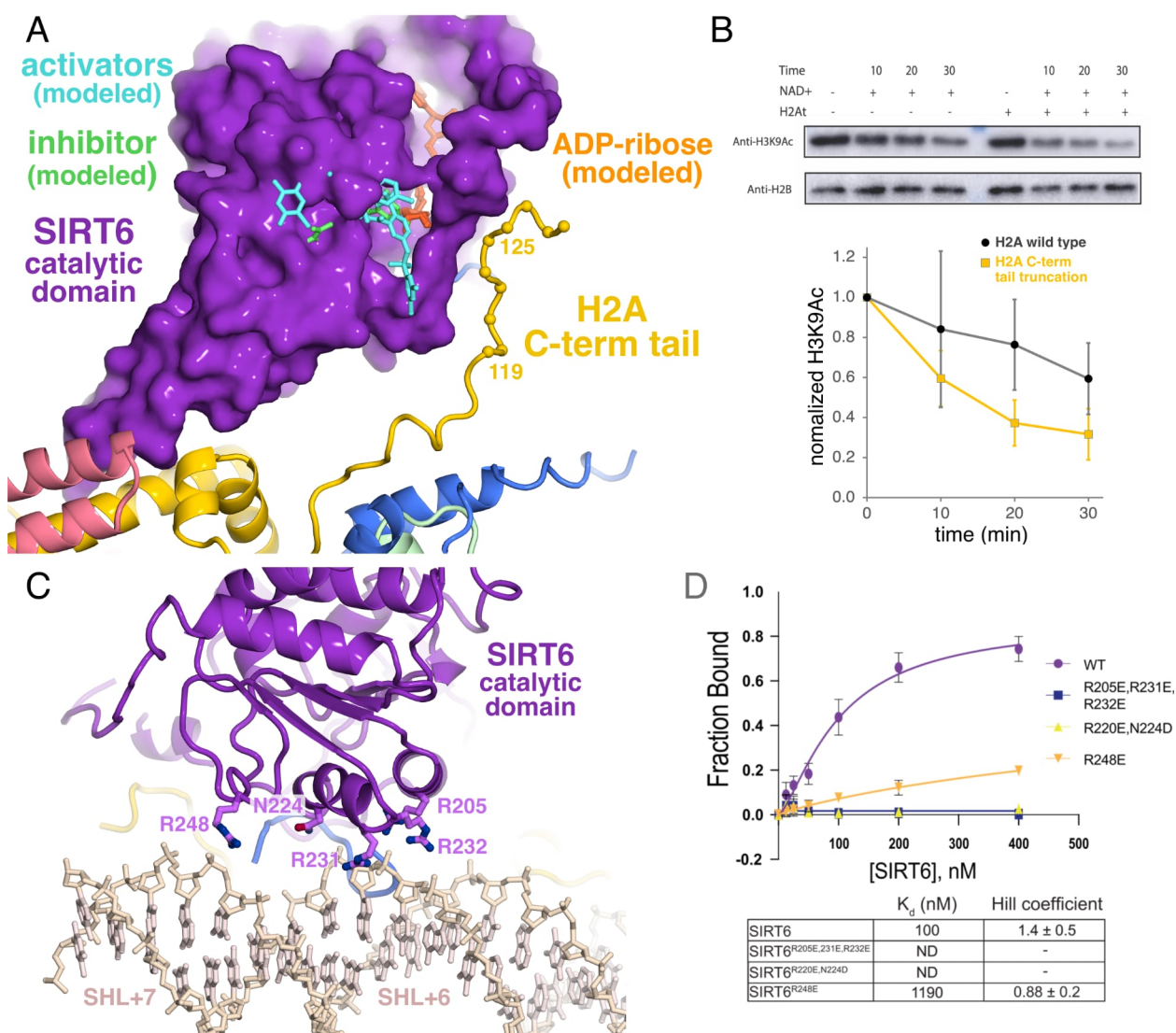
59
60
61
62
63

Fig. 1: Overview of SIRT6/nucleosome structure. (A) 3.07 Å cryo-EM Coulomb potential density map of structure, (B) Cartoon representation of structure.



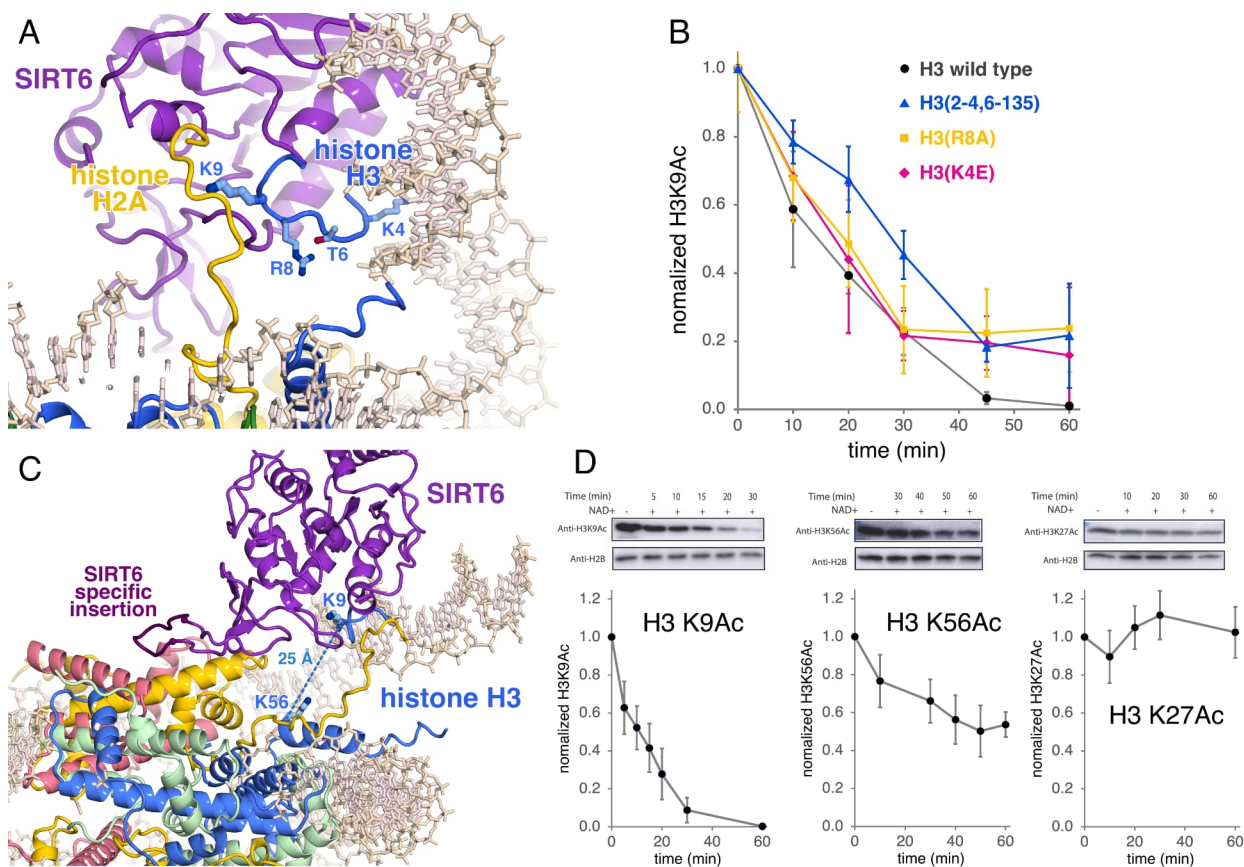
64
65
66
67
68
69
70
71
72

Fig. 2: Interactions of SIRT6 zinc-binding domain with nucleosome acidic patch. (A) Cartoon representation of SIRT6 zinc-binding domain with histone dimer acidic patch, (B) Quantification of nucleosome binding assay for wild type and mutant SIRT6, (C) SIRT6 H3K9Ac deacetylase assay for wild type and R175A SIRT6 normalized against H2B with representative Western blot (top) and plot showing standard deviation error bars with $n = 3$ (bottom).



73
74
75
76
77
78
79
80
81
82
83
84
85
86
87

Fig. 3: Inhibitory interactions of histone H2A C-terminal tail near SIRT6 allosteric binding pocket, and nucleosomal DNA interactions of SIRT6 catalytic domain with nucleosomal DNA. (A) The histone H2A C-terminal binds to SIRT6 proximal to allosteric activators (MDL-801, modeled from two different structures (PDB 5Y2F and 6XV1) and an allosteric inhibitor (catechin gallate, PDB 6QCJ). The modeled product analog, 2'-O-acyl-ADP-ribose, adopts a well-defined conformation in these three SIRT6-allosteric effector structures. The C α positions of the H2A C-terminal residues 119-128 are shown as yellow spheres. (B) Deletion of the H2A C-terminal tail enhances SIRT6 nucleosomal H3K9Ac deacetylase activity (normalized against histone H2B). Representative Western blot data (top) and plot for HDAC assays (n=3) shown. (C) Interactions of SIRT6 catalytic domain with nucleosomal DNA. Same color code as for Fig. 2a. (D) Quantification of nucleosomal binding assay for wild type and SIRT6 mutated in DNA-binding residues



88
89
90
91
92
93
94
95
96

Fig. 4: SIRT6 nucleosomal substrate specificity. (A) Cartoon and stick representation of SIRT6 binding of H3 tail around substrate residue K9. (B) Point mutations and deletions of H3 tail residues that interact SIRT6 adversely affect SIRT6 nucleosomal histone H3K9Ac deacetylase activity. (C) Cartoon and stick representation of SIRT6/nucleosome complex shows that histone H3 K56 is exposed but is at least 25 Å from H3 K9 and the SIRT6 catalytic site. (D) SIRT6 HDAC activity on nucleosomal histone H3 K9, K56 and K27.

Supplementary Materials for

Cryo-EM structure of the human Sirtuin 6-nucleosome complex

Un Seng Chio^{1,2,3†}, Othman Rechiche^{1,2,†}, Alysia R. Bryll^{4,5†}, Jiang Zhu^{1,2}, Jessica L. Feldman⁴,
Craig L. Peterson^{4*}, Song Tan^{1,2*}, Jean-Paul Armache^{1,2*}

Correspondence to:

craig.peterson@umassmed.edu

sxt30@psu.edu

jza449@psu.edu

This PDF file includes:

Figs. S1 to S5

Tables S1 to S2

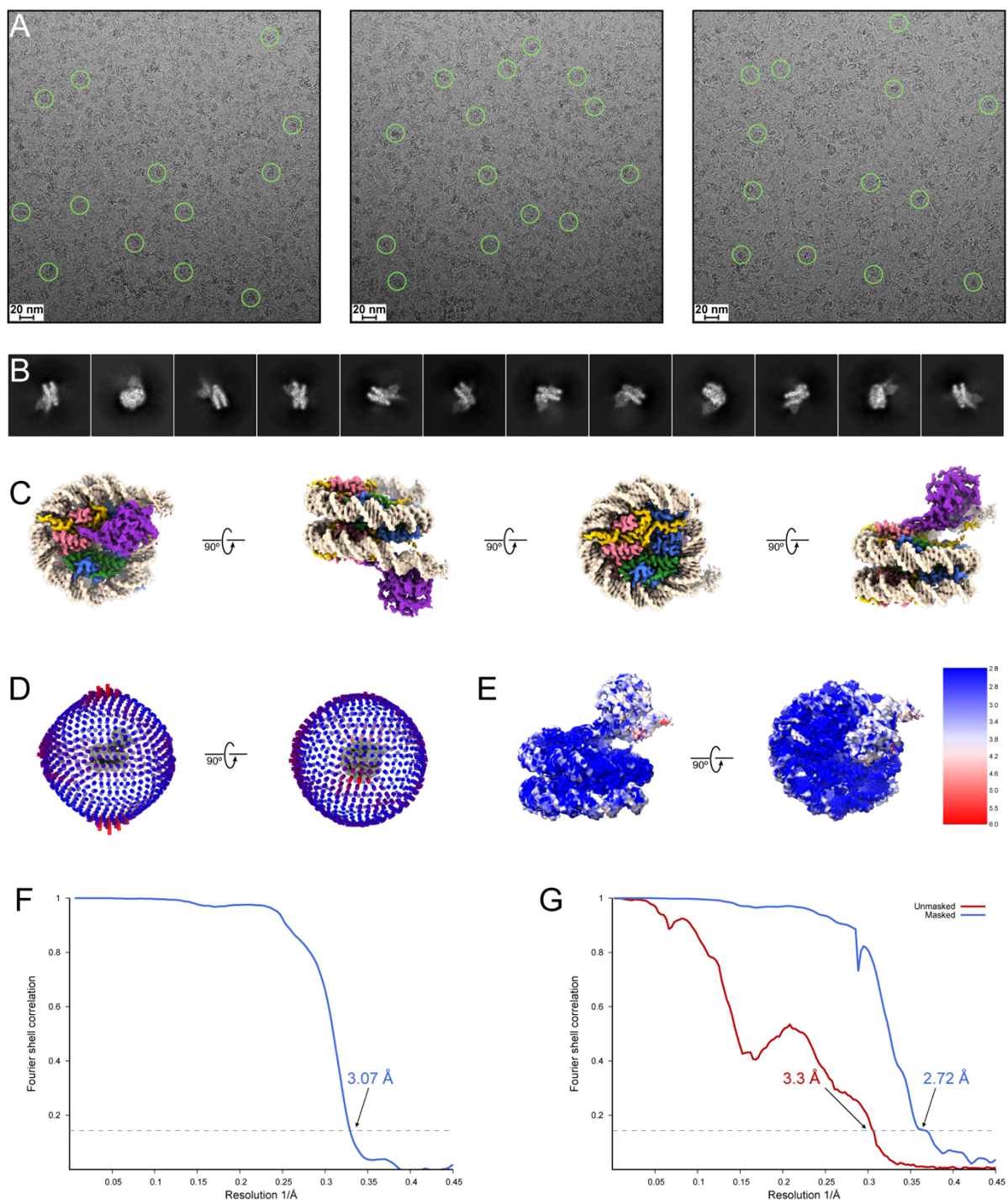


Fig. S1. Cryo-EM studies of SIRT6 bound to 172 bp nucleosome. **(A)** Representative motion-corrected micrographs from the SIRT6 bound to 172 bp nucleosome dataset. **(B)** Representative 2D classes of SIRT6 bound to 172 bp nucleosome. **(C)** Four different views of the cryo-EM map of SIRT6 bound to 172 bp nucleosome generated with cisTEM. The structure is color-coded with histone H3 in light blue, histone H4 in light green, histone H2A in light yellow, histone H2B in light pink, DNA strands in light/dark gray, and SIRT6 in dark blue. **(D)** Angular distribution of particles used to generate the cryo-EM map of SIRT6 bound to 172 bp nucleosome in cisTEM.

(E) Cryo-EM map of SIRT6 bound to 172 bp nucleosome generated in cisTEM colored by estimated local resolution determined with FSC = 0.143 cutoff in cryoSPARC. **(F)** Fourier shell correlation curve between two half-maps for the SIRT6 bound to 172 bp nucleosome refinement determined by cisTEM. **(G)** Unmasked (red) and masked (blue) Fourier shell correlation curves between two independent half-maps for the SIRT6 bound to 172 bp nucleosome refinement determined by cryoSPARC.

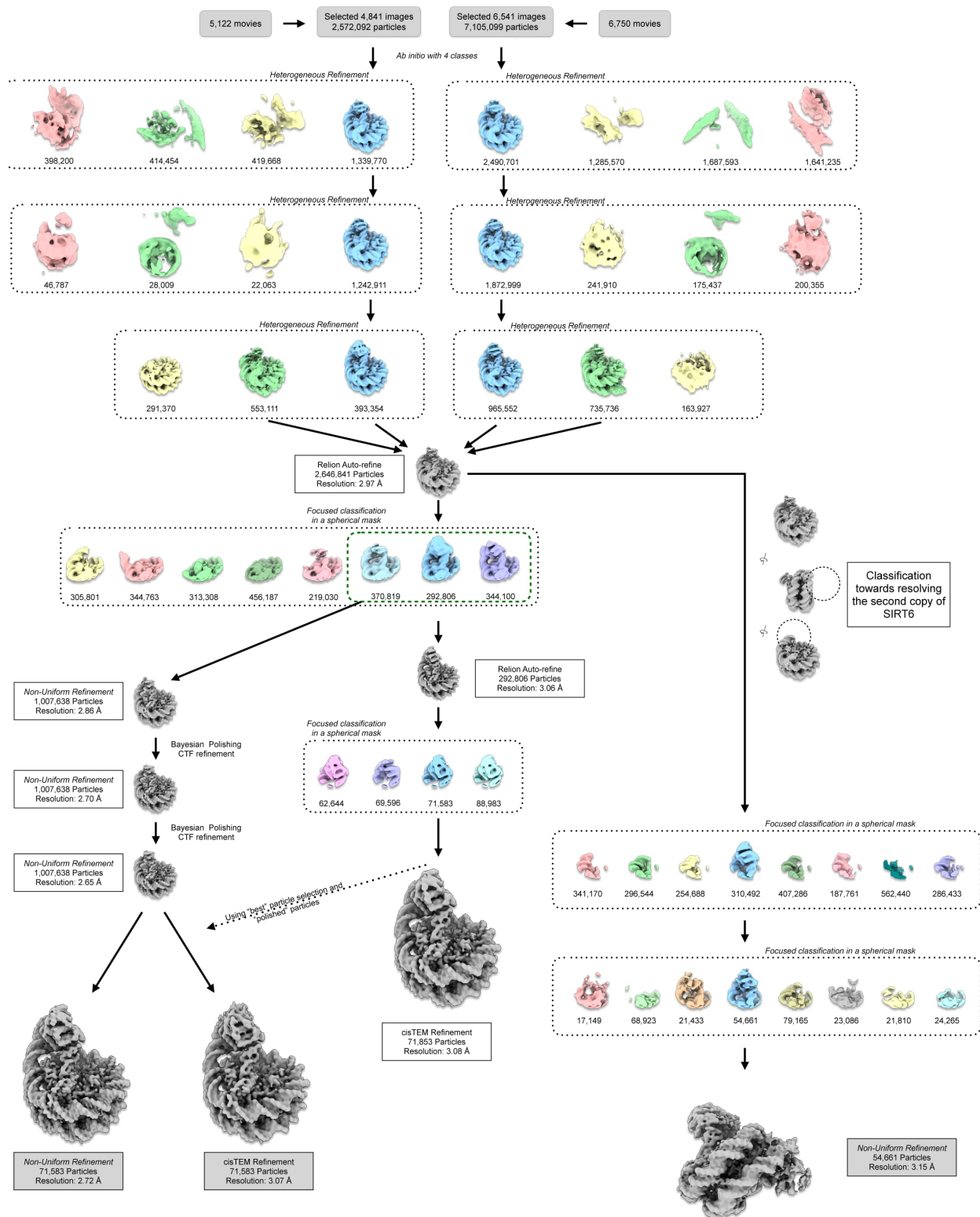


Fig. S2: Data processing for SIRT6 bound to 172 bp nucleosome. Flowchart for cryo-EM data processing of the SIRT6 bound to 172 bp nucleosome datasets as described in Methods. Initial processing steps were performed in cryoSPARC with the number of particles moving into each

step noted. Focused classifications without alignment were performed in RELION-3.1 to improve SIRT6 density. Rounds of Bayesian polishing and CTF refinement were also performed in RELION-3.1 to improve the overall map. Final refinements were performed in both cryoSPARC and cisTEM.

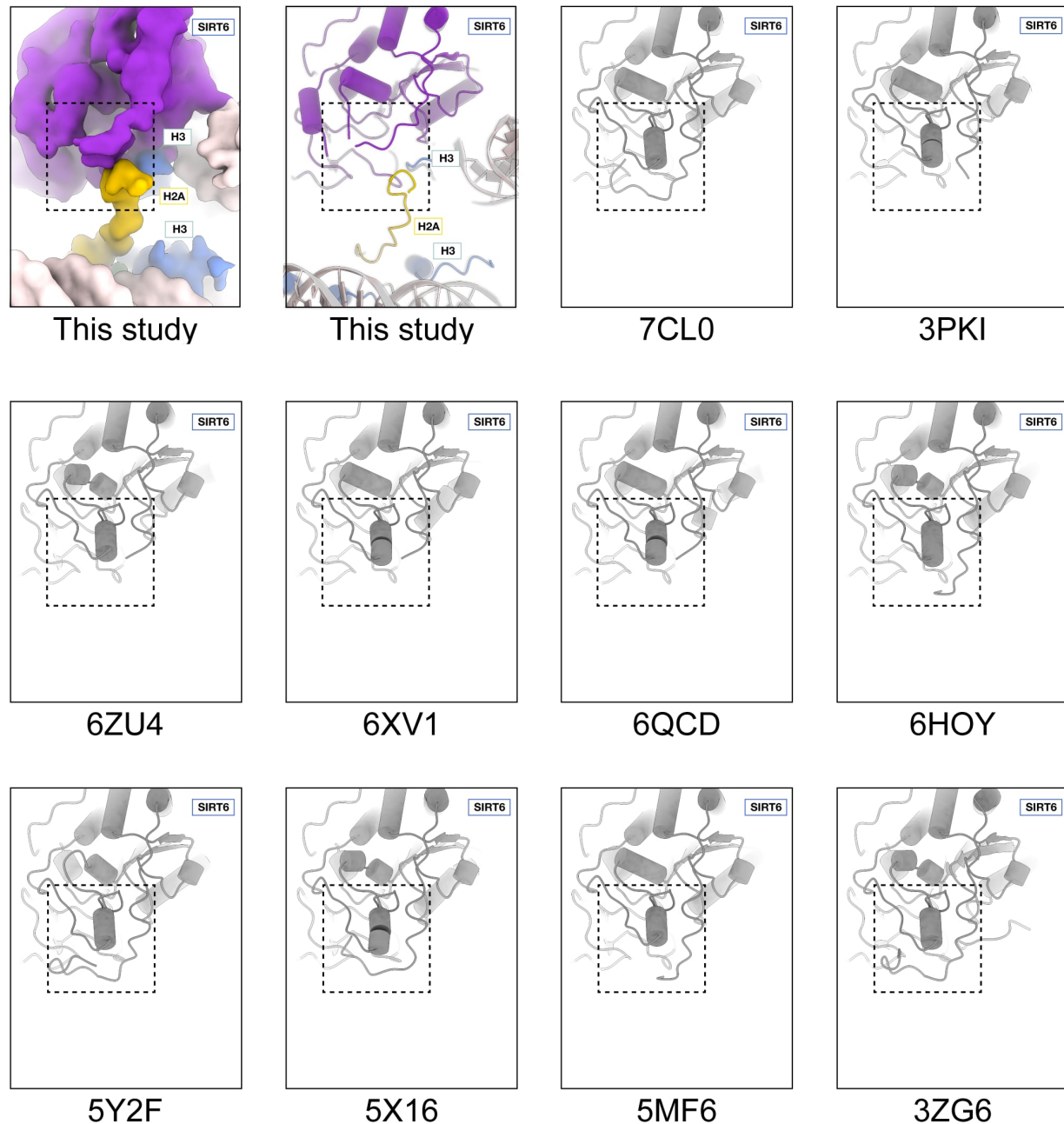


Fig. S3: Comparison of SIRT6 residues 64-80 between structures. SIRT6 is missing density for residues 64-80 in our structure (“this study” panels) suggesting the region is disordered. SIRT6 crystal structures have their PDBID codes indicated underneath. Residues 64-80 are ordered and form a small alpha-helix in all crystal structures of SIRT6 with ADP-ribose.

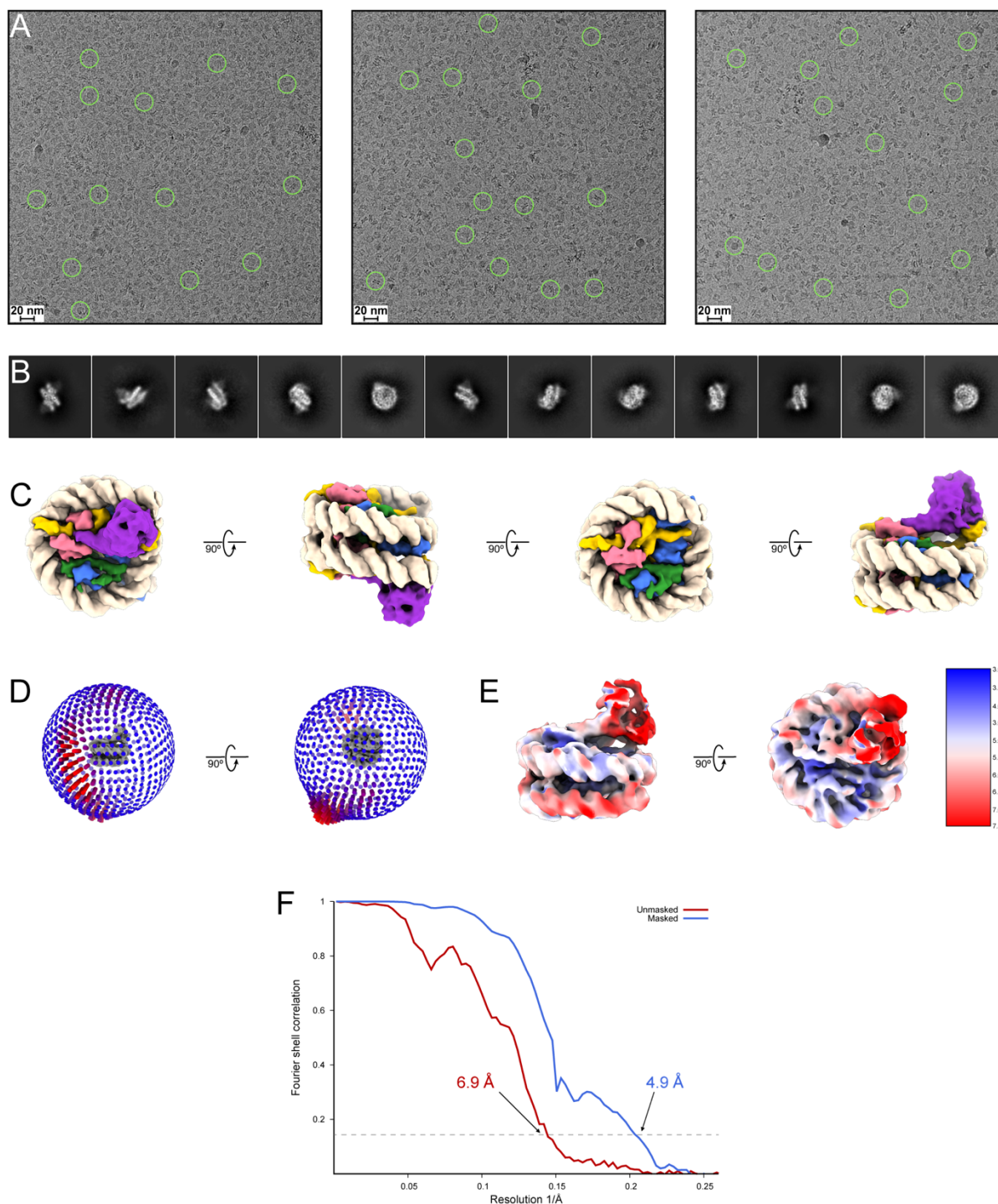


Fig. S4: Cryo-EM studies of SIRT6 bound to 147 bp nucleosome. **(A)** Representative motion-corrected micrographs from the SIRT6 bound to 147 bp nucleosome dataset. **(B)** Representative 2D classes of SIRT6 bound to 147 bp nucleosome. **(C)** Four different views of the cryo-EM map of SIRT6 bound to 147 bp nucleosome. The structure is color-coded with histone H3 in light blue, histone H4 in light green, histone H2A in light yellow, histone H2B in light pink, DNA strands in light/dark gray, and SIRT6 in dark blue. **(D)** Angular distribution of particles used to generate the cryo-EM map of SIRT6 bound to 147-base pair nucleosome. **(E)** Cryo-EM map of SIRT6 bound

to 147 bp nucleosome colored by estimated local resolution determined with FSC = 0.143 cutoff in cryoSPARC. **(F)** Unmasked (red) and masked (blue) Fourier shell correlation curves between two independent half-maps for the SIRT6 bound to 147 bp nucleosome refinement determined by cryoSPARC.

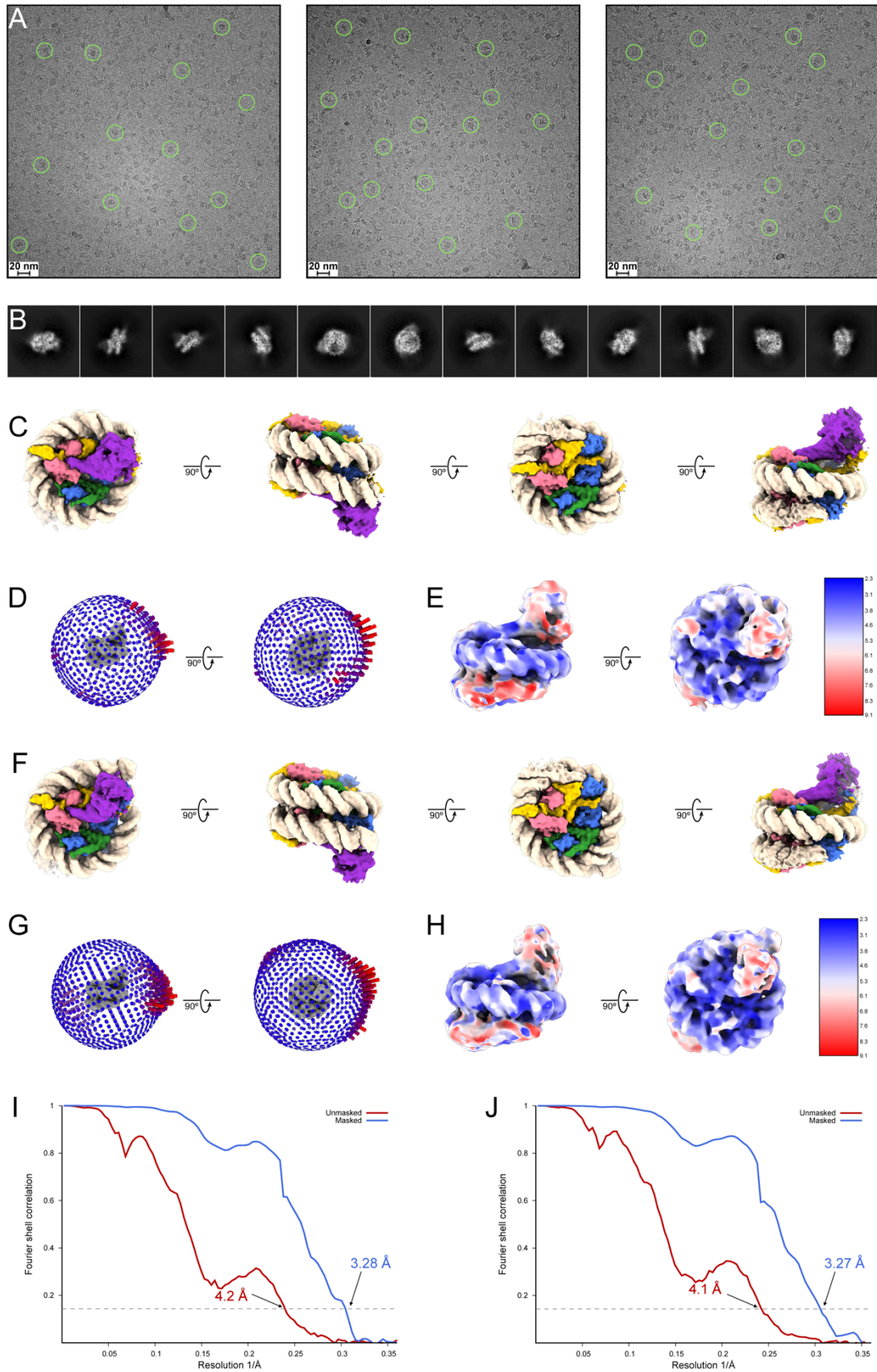


Fig. S5: Cryo-EM studies of SIRT6 bound to 145 bp nucleosome. **(A)** Representative motion-corrected micrographs from the SIRT6 bound to 145 bp nucleosome dataset. **(B)** Representative 2D classes of SIRT6 bound to 145 bp nucleosome. **(C)** Four different views of one cryo-EM map determined of SIRT6 bound to 145 bp nucleosome. The structure is color-coded with histone H3 in light blue, histone H4 in light green, histone H2A in light yellow, histone H2B in light pink, DNA strands in light/dark gray, and SIRT6 in dark blue. **(D)** Angular distribution of particles used to generate the first cryo-EM map of SIRT6 bound to 145 bp nucleosome. **(E)** The first cryo-EM map of SIRT6 bound to 145 bp nucleosome colored by estimated local resolution determined with FSC = 0.143 cutoff in cryoSPARC. **(F)** Four different views of the second cryo-EM map determined of SIRT6 bound to 145 bp nucleosome. The structure is color-coded as in (C). **(G)** Angular distribution of particles used to generate the second cryo-EM map of SIRT6 bound to 145 bp nucleosome. **(H)** The second cryo-EM map of SIRT6 bound to 145 bp nucleosome colored by estimated local resolution determined with FSC = 0.143 cutoff in cryoSPARC. **(I)** Unmasked (red) and masked (blue) Fourier shell correlation curves between two independent half-maps for the first SIRT6 bound to 145 bp nucleosome refinement determined by cryoSPARC. **(J)** Unmasked (red) and masked (blue) Fourier shell correlation curves between two independent half-maps for the second SIRT6 bound to 145 bp nucleosome refinement determined by cryoSPARC.

Table S1. Summary for cryo-EM data collection and refinement

Sample	Sirt6-145 bp nucleosome	Sirt6-147 bp nucleosome	Sirt6-172 bp nucleosome
Instrument	Titan Krios	Titan Krios	Titan Krios
Voltage (kV)	300	300	300
Energy filter slit width (eV)	20	-	20
Magnification	81,000	59,000	81,000
Total electron dose (e ⁻ /Å ²)	50	58.19	50
Camera	Gatan K3	FEI Falcon3	Gatan K3
Camera mode	Super Resolution	Counting	Super Resolution
Image pixel size (Å)	0.5295	1.14	0.54
Reconstruction pixel size (Å)	1.059	1.14	1.08
Defocus range (µm)	-0.8 to -2.2	-0.5 to -2.5	-1.0 to -2.2
Number of images	7,730	524	11,872
Number of frames per image	50	44	40
Data collection software	SerialEM	FEI EPU	Gatan Latitude S
Motion correction software	UCSF MotionCor2 v1.4.1	CryoSPARC v2.31 Patch Motion Correction	UCSF MotionCor2 v1.4.1
Starting number of particles	2,351,642	398,186	12,821,862
Particles in final reconstruction	31,802 / 34,737	40,834	71,603
Final resolution at 0.143 FSC cutoff (Å)	3.28 / 3.27	4.90	3.07

Table S2. Model refinement statistics

Sample name	Sirt6-nucleosome model
Model composition	
..Atoms	14 396
..Residues: Protein/Nucleotide	1 067/300
Model refinement software	phenix.real_space_refinement
Model-vs data	
CC (mask)	0.72
CC (box)	0.67
Resolution estimates (Å)	
FSC model (0.143/0.5) Masked	3.1 / 3.3
FSC model (0.143/0.5) Unmasked	3.2 / 3.9
ADP (B-factors, min/max/mean)	
Protein	12.67 / 184.25 / 79.86
Nucleotide	33.03 / 219.03 / 57.20
ADP (B-factors, min/max/mean)	
Protein	12.67 / 184.25 / 79.86
Nucleotide	33.03 / 219.03 / 57.20
Bonds (RMSD)	
Length (Å) (# > 4σ)	0.004
Angles (°) (# > 4σ)	0.823
MolProbity score	1.71
Clash score	8.01
Rotamer outliers (%)	0.12
Cβ outliers (%)	0.00
Ramachandran values (%)	
Outliers	0.86
Allowed	3.16
Favored	95.97